11654 *J. Phys. Chem. A* **2006,** *110,* 11654−11664

Diffusion Kinetics for Methanol in Polycrystalline Ice

Patrick Marchand, Samuel Riou, and Patrick Ayotte*

Département de Chimie, Université de Sherbrooke, 2500 Boulevard Université, Sherbrooke, Québec J1K 2R1, Canada

Received: June 29, 2006; In Final Form: August 16, 2006

Quantitative analyses of the isothermal desorption kinetics from methanol-doped H_2O films on Pt(111) reveal that transport kinetics for CH_3OH in polycrystalline ice are much slower than previously reported. They also indicate that MeOH displays first-order desorption kinetics with respect to its instantaneous surface concentration below 0.1 mole fraction in ice. These observations allow isothermal desorption rate measurements to be interpreted in terms of a depth profiling analysis providing one-dimensional concentration depth profiles from methanol-doped polycrystalline ice films. Using a straightforward approach to inhibit ice sublimation, transport properties are extracted from the evolution of concentration depth profiles obtained after thermal annealing of binary ice films at high temperature. Heterodiffusion coefficients for methanol in polycrystalline (cubic) ice I_c films are reported for temperatures between 145 and 195 K and for concentrations below 10^{-3} mole fraction. Finally, diffusion kinetics for methanol in ice are shown to display a very strong concentration dependence that may contribute, in addition to variations in laboratory samples microstructure, to the disagreements reported in the literature regarding the transport properties of ice.

I. Introduction

Natural ice is a ubiquitous and continuously evolving molecular solid that presents heterogeneities on several length scales, ranging from molecular to kilometers.[1] These features represent a considerable challenge toward decoding the planetary atmospheric archives trapped in the polar ice caps.[2] Accordingly, the interpretation of climate proxies from ice cores has recently sparked renewed interest in the complex transport properties of ice.[3,4] Furthermore, as the latter are strongly coupled to the bulk uptake and interfacial reaction kinetics on ice particles and snow,[5,6] a better understanding of these phenomena is also crucial to help quantify the role played by ice in determining the chemical composition of the atmosphere[7] and the polar boundary layer.[8,9]

It has thus been long recognized that the composition, structure, and morphology of ice particles and snowflakes encode chemical and physical clues of the environments in which they were formed and subsequently evolved. As they precipitate and accumulate on seasonally and permanently snow-covered areas, they form vertically stratified deposits within the snow pack. The complex transition from this initially highly porous, freshly fallen snow deposit, to the highly connected percolating pore structure of the fern, to dense polycrystalline ice still remains poorly understood. This formidably complex process controls the early-time evolution of the initially vertical concentration profiles. A quantitative understanding of aging processes in natural snow, such as sublimation and condensation, vapor and bulk diffusion, metamorphism, densification, creep, and flow, is thus required to properly date and interpret the concentration profiles retrieved from ice cores as well as improve our understanding of the role played by the snow pack in atmospheric chemistry phenomena at the polar boundary layer.

The various impurity species used as climate proxies display complex interactions with the ice matrix that are controlled by their molecular properties, their chemical and physical state, but also the ice composition, morphology, and microstructure. Consequently, these features will also determine the transport and equilibrium properties of impurity molecules trapped within the ice matrix: from their initial spatial distribution within snow particles in the atmosphere to whether they will evolve to form microinclusions,[10] collect at grain boundaries,[11] or disperse more or less homogeneously within the ice crystallites that compose natural ices. Detailed knowledge of these parameters, as provided from analyses of natural samples, is thus required in order to guide laboratory investigations and provide environmentally meaningful kinetic parameters from model systems.

Various experimental approaches have been proposed to probe the transport properties, and in particular the molecular diffusion kinetics, for various impurity molecules in artificial ice samples.[12−20] The acute and complex dependence of the phase, morphology, and microstructure of laboratory ices on preparation methods (vapor condensation or crystallization from the melt)[19−21] and growth conditions (flux/pressure,[22] temperature,[23] angle of incidence,[24] nature of the heterogeneous substrate,[25−28] etc.) and the great difficulties to experimentally quantify defect densities (dislocations, interstitials, vacancies, Bjerrum defects, etc.)[29] are all factors that severely limit meaningful comparisons between the results from these different studies. Compounded with our limited ability to characterize accurately and nondestructively the morphology and microstructure of this delicate material, these considerations contribute to the large discrepancies between the results obtained from laboratory ice samples prepared by very different methods. Accordingly, uncontrolled and poorly characterized defects are often invoked as a possible source for the irreproducibility of bulk diffusion measurements in otherwise identically prepared macroscopic samples even within a single investigation[19,30] let alone comparing different studies. As a specific example, the

---

* To whom correspondence should be addressed. Phone: 819-821-7889. Fax: 819-821-8017. E-mail: Patrick.Ayotte@USherbrooke.ca.

10.1021/jp0640878 CCC: $33.50

large scatter in the diffusion coefficients for HCl in ice reported by different authors (i.e., 8 orders of magnitude disagreement at 185 K)[12,13,16] obscures a consistent description of the phenomenon and also highlights our poor understanding of the factors that control transport properties in ice.

A few distinct diffusion mechanisms for a series of atomic and molecular species in ice I_h were recently described using molecular dynamics simulations.[31−33] Several features of these mechanisms were specific to the chemical nature of the impurity species yielding quite different kinetics. For example, the kinetics for an interstitial mechanism were reported to be a very sensitive function of the size of the diffusing species.[31,34] In contrast, a recent survey of diffusion coefficients measured in laboratory ice using laser-induced thermal desorption (LITD) depth profiling[21] reported that the transport kinetics for acetic and formic acid, methanol, and HCl are all quite similar. This suggests that molecular transport of these very chemically different species in ice may proceed by a common mechanism, presumably a vacancy-mediated mechanism.[21] However, it has been recently argued[15−18] that the diffusion coefficients reported by Livingston et al.[21] were too large to be interpreted as molecular diffusion in crystalline ice. This statement[15−18] rested principally on the suggestion that the high impurity concentrations used in these (and other) experiments might have yielded the formation of (amorphous or crystalline) hydrates within these mixed molecular solids. The reported diffusion coefficients were thus hypothesized[15−18,21] to most likely correspond to transport through these hydrate phases rather than molecular heterodiffusion within ice. This strong implicit dependence of the transport kinetics on impurity concentration is thought to be another important source of disagreement between the various reports. While the limited detection efficiency of these bulk transport measurements required rather high impurity concentrations to be used,[21] several uptake kinetics measurements also suffered from the high impurity partial pressures used that may have exceeded their solubility in ice, effectively “melting” the superficial layers.[12,13,17,18,35] For example, it is now relatively well understood[12,13,17,18,35] that despite the very small solubility of HCl in ice, a relatively concentrated (amorphous or crystalline hydrate or supercooled solution) superficial layer may form during gas uptake at low temperature. Therefore, the apparent uptake kinetics in ice can be very different than those for bulk heterodiffusion due to the strong dependence of the interfacial HCl concentration boundary conditions upon the various conditions of temperature and pressure of uptake experiments. Great care must thus be taken in the analysis and interpretation of laboratory data as high temperatures and concentrations may promote segregation, phase separation, and formation of various phases (i.e., stable or metastable liquids, amorphous, or crystalline hydrates) in impure ices.

As a result, the best approach to experimentally probe molecular diffusion kinetics in ice and the applicability of laboratory results to interpret natural phenomena remains the subject of debate.[14,16] It is clear however that impurity concentrations near the solid−solution regime need to be achieved in order to inhibit phase separation and crystallization of the various hydrates during diffusion kinetics measurements in laboratory ices. In addition, adequate characterization of the samples microstructure is highly desirable as identification of the coexisting solid phases as well as determination of defect densities, in particular those of grain boundaries, could improve our interpretation of the kinetics and, consequently, our description of a diffusion mechanism. Furthermore, the identity of the crystalline ice polymorph (i.e., cubic vs hexagonal) formed by vapor deposition on a substrate, either by condensation at higher temperature or by thermal annealing of a microporous thin film deposit, remains controversial.[23,36−38] It is thus imperative to identify the solid phase in which the transport kinetics are being measured (i.e., which ice polymorph or crystalline hydrate).

Heterodiffusion coefficients for methanol in submicrometer thick laminate ice films are reported here for mole fractions under 10^{-3} and temperatures in the 145−195 K range. Methanol was selected based on the relative simplicity of the MeOH−H_2O binary phase diagram[39] (but despite uncertainties regarding the possibility that it may form a clathrate hydrate phase),[40,41] the availability of diffusion coefficients in the literature,[21] as well as general current interest in the interaction of volatile organic compounds with ice.[9] After synthesizing the samples using molecular beam techniques, isothermal desorption mass spectrometry experiments were performed. Methanol desorption from ice films was observed to follow first-order kinetics with respect to its instantaneous surface concentration below ca. 10% mole fraction (section III.A). Given the very slow transport observed for methanol in polycrystalline ice samples and assuming layer-by-layer sublimation of the methanol-doped H_2O films (which display near zero-order H_2O desorption kinetics), their time-dependent isothermal desorption rates are interpreted in terms of one-dimensional concentration depth profiles. As diffusion rates for this molecule in ice are much slower than the H_2O desorption rates from ice, a simple experimental procedure was devised to suppress sublimation of the samples during annealing at the high temperatures (or the long annealing times) required to promote molecular transport. Heterodiffusion coefficients are extracted by numerically solving the one-dimensional diffusion equation by performing a convolution integral over the initial concentration profile. The resulting Fickian profiles are then least-squares fitted to the diffusionally broadened concentration profiles obtained after thermal annealing of the thin laminated film samples (section III.B). By comparing our kinetic parameters with those reported previously using a similar method (i.e., LITD) but much greater amounts of methanol,[21] a very strong dependence of the apparent diffusion kinetics upon MeOH concentration (i.e., the thickness of the impurity layer in the laminate structure) is revealed. The concentration of methanol is thus confirmed to have a very large impact on its transport kinetics in ice. Analysis of the microstructure using transmission electron microscopy (TEM) and identification of the coexisting solid phases by electron diffraction reveal that the thin ice films used in the transport kinetics measurements are most probably polycrystalline (cubic) ice I_c (section III.C). Besides polycrystalline ice I_c and I_h, no other crystalline phase (i.e., hydrates) could be observed in the TEM experiments for films having similar methanol concentrations that underwent similar thermal histories to those used in the diffusion kinetics measurements.

II. Experimental Methods

The experimental setup is shown schematically in Figure 1. Binary ice films (up to a few thousand monolayers thick) were grown in UHV (P1 $< 10^{-9}$ Torr) by vapor deposition on a Pt(111) single-crystalline substrate (1 cm diameter disk, 1 mm thick) using either background deposition or molecular beam dosing. The platinum substrate was fixed to a sample holder coupled to a closed-cycle helium cryostat (APD cryogenics, model 202B) that was mounted on a three-axes sample manipulator (*XYZ*) and a differentially pumped rotary flange allowing control of the polar angle. The sample temperature

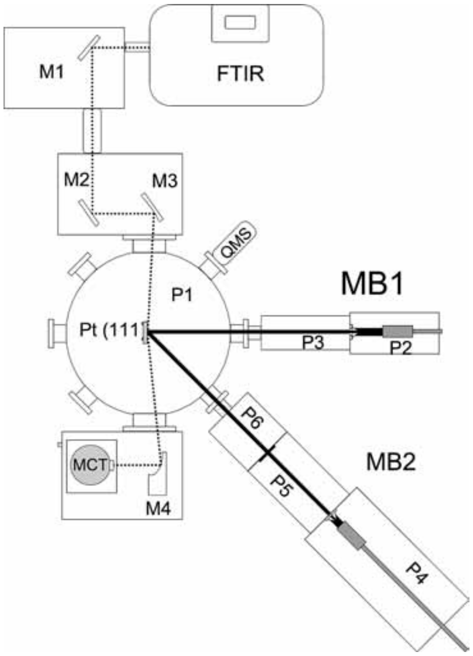

Figure 1. Schematics of the experimental apparatus (see text for detailed description). Principal constituents are the UHV analysis chamber [P1] that houses the Pt(111) substrate. It is equipped with a doubly differentially pumped [P2−P3] molecular beam doser [MB1], a triply differentially pumped [P4−P6] molecular beam source [MB2], a quadrupole mass spectrometer [QMS], and an ion sputter gun [not shown]. Two differentially pumped optical ports and steering optics [M1−M4] provide in situ reflection−absorption infrared spectroscopy capabilities using a commercial interferometer [FTIR] and a infrared detector [MCT].

was controlled by resistive heating from ~35 to 1300 K and measured with a type K thermocouple spot-welded to the unpolished backside of the Pt(111) substrate. Absolute temperature calibrations were performed using multilayer desorption of various species (Kr, H_2O, ...) from the substrate surface.[42] The accuracy of the absolute temperature was estimated to be ±2 K, but the relative temperature could be controlled to better than ±50 mK using a PID algorithm [Instrument Development Laboratory (IDL), Pacific Northwest National Laboratory (PNNL)]. Standard cleaning procedures including ion sputtering (VG EX03; Ar^+, 1.5 kV, 18 μA, 20 min) and annealing in UHV (1150 K, 3 min) were performed daily. Surface preparation procedures were verified using thermal desorption mass spectrometry (TDMS) of a few monolayers of water (and of other species) for which thermal desorption spectra from clean and atomically ordered Pt(111) substrates have been reported in the literature.[43] TDMS analyses were performed using a typical linear ramp rate of 0.5 K/s and a quadrupole mass spectrometer (Balzers Prima 200, 1−100 amu) positioned in the line-of-sight of the sample. Data acquisition for TDMS experiments was performed with the modular architecture software Surf-O-Matic (IDL, PNNL).

Two molecular beam sources (MB1 and MB2, Figure 1) were used to grow thin films of various mixed molecular solids. A doubly differentially pumped molecular beam doser (MB1; P2−P3) delivered an effusive beam of H_2O vapor with a maximum flux of ca. 10^{14} molecules cm^{-2} s^{-1} (~0.1 ML/s for H_2O). A triply differentially pumped molecular beam source (MB2; P4−P6) generated an effusive beam with a maximum flux of ca. 4×10^{13} molecules cm^{-2} s^{-1} (~0.04 ML/s for H_2O). The two coplanar molecular beams (separated by a 45° polar angle) were coincident on the sample, which allowed growth of layered (by sequential dosing) or homogeneous (by simultaneous dosing) binary molecular films onto the substrate. For the experiments reported here, mixed ice films were grown using nanopurified water (MilliQ, 18 MΩ) and HPLC-grade methanol (ACP Chemical, 99.8%), which were thoroughly degassed by repeated freeze−pump−thaw cycles. The flux of each molecular beam source, J in ML/s, is calibrated against the respective saturated monolayer (ML) coverages on Pt(111) using TDMS of precisely controlled quantities of adsorbed MeOH or H_2O[44,45] or the beam reflection technique of King and Wells.[46] The coverage or dose, θ in ML, is the product of the molecular beam flux and dose time as the sticking and condensation coefficients of H_2O and MeOH on Pt(111) and ice are unity for the conditions used during sample preparation. Instantaneous sample compositions were reported in monolayer fractions which are defined as the ratio of the (time-dependent) instantaneous MeOH coverage, $\theta_{MeOH}(t)$, to the (time-dependent) instantaneous total coverage, $\theta_{H2O}(t) + \theta_{MeOH}(t)$ {e.g., instantaneous monolayer fraction = $\theta_{MeOH}(t)/[\theta_{H2O}(t) + \theta_{MeOH}(t)]$}. This definition is used throughout to describe the continuously evolving overall bulk composition as well as the instantaneous composition of the surface layer. Instantaneous coverages were evaluated by integrating the water and methanol desorption fluxes, providing an estimate of their continuously evolving respective coverages. The monolayer fractions were converted to approximate mole fractions [e.g., $x_{MeOH} = n_{MeOH}/(n_{H2O} + n_{MeOH}) = \theta_{MeOH}\sigma_{MeOH}/(\theta_{H2O}\sigma_{H2O} + \theta_{MeOH}\sigma_{MeOH})$] using the relative surface (2D) densities for saturated monolayers of MeOH (σ_{MeOH}) and H_2O (σ_{H2O}) on clean Pt(111).[44,45] At the lowest concentrations used in this study, the ratio of the monolayer fraction to the mole fraction is close to the ratio in the monolayer surface densities for MeOH and H_2O (i.e., $\sigma_{H2O}/\sigma_{MeOH} \approx 1.86$).[44,45]

Reflection−absorption infrared spectroscopy (RAIRS) was performed in situ at grazing angle (~85°) in the plane defined by the two molecular beams and the quadrupole mass spectrometer using unpolarized light from a commercial FTIR spectrometer (ThermoNicolet, Nexus 670). The external beam path with all the optics (M1−M4), the spectrometer (FTIR), and the mercury−cadmium−telluride detector (MCT) were enclosed within custom plexiglass housings and purged from atmospheric contaminations. The infrared beam was coupled to the UHV system through differentially pumped KBr windows, allowing a useful spectral coverage from 650 to >7000 cm^{-1}. In this grazing angle geometry, absorbance spectra from thin films include contributions from absorption within the sample as well as modulation of reflectivity and optical interference effects (i.e., Fresnel spectra).[47,48]

The molecular transport kinetics for relatively large molecules in ice are very slow. Therefore, to promote diffusion of methanol in thin ice films, samples need to be annealed to rather high temperatures where H_2O desorption becomes substantial.[49] A simple procedure was devised to prevent sublimation of the sample, thereby enabling thermal annealing in the crucial 180−195 K temperature range. A gold-plated glass microscope slide was mounted on a single-tilt stage installed on a linear feed through allowing control over its height and inclination inside the UHV analysis chamber. The platinum substrate can be positioned parallel to and within a few tens of micrometers of the microscope slide (using the *XYZ* and polar angle control of the sample manipulator) by monitoring the capacitance between the substrate and the gold plating. This plane capacitor geometry causes readsorption of the H_2O molecules desorbing from the ice film by maintaining a relatively high H_2O partial vapor pressure over the sample surface. After a thermal treatment of several minutes at the selected annealing temperature (in the

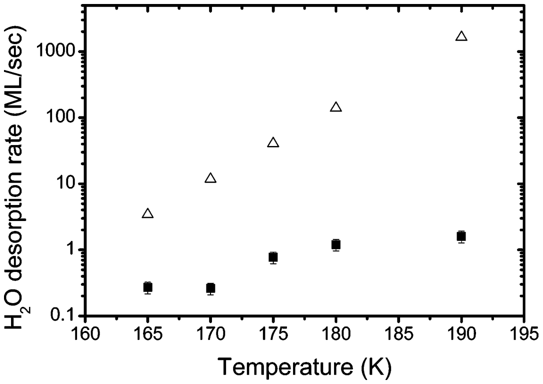

Figure 2. H_2O desorption rates from ice (△),[50] and effective H_2O desorption rates with the sample positioned in front of the gold-plated microscope slide (■) as a function of substrate temperature.

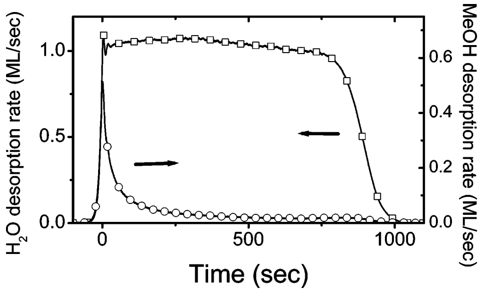

Figure 3. Isothermal desorption rates for H_2O (□, left ordinate) and MeOH (○, right ordinate) at 160 K for a 880 ML thick binary film sample grown at 80 K having an initially homogeneous bulk MeOH concentration of (0.055 ± 0.010) monolayer fraction (see text).

145−195 K range), the amount of ice left on the substrate was measured using TDMS and FTIR. The amount of material lost during annealing was evaluated and expressed as an effective desorption rate (ratio of the number of ML lost to the annealing time). H_2O desorption rates from ice (open triangles)[49,50] and the effective desorption rates in the presence of the glass plate (black squares) are shown as a function of annealing temperature in Figure 2. At 190 K, the effective desorption rate was measured to be 3 orders of magnitude smaller than the desorption rate from ice. However, the apparent temperature dependence of the decrease in desorption rate caused by the glass plate and the scatter in the experimental data both reflect the sensitivity of this inhibiting effect on the positioning of the sample inside the UHV chamber. This simple procedure has been used to inhibit H_2O sublimation during the prolonged annealing of the samples at the relatively high temperatures (or long annealing times) required to cause measurable diffusion of methanol in ice.

Electron diffraction and microscopic observation of thin (pure and mixed) ice films were performed on a Hitachi H7500 TEM using a custom LN_2-cooled cryogenic sample manipulator (Gatan). Specimens were prepared in a turbo-pumped custom environmental chamber mounted directly on the TEM goniometer, thereby eliminating atmospheric contamination during sample transfer to the microscope. Thin films were grown on a commercial amorphous carbon or silica film TEM substrate (SPI supplies Inc.) by background deposition using the vapor pressure of thoroughly degassed aqueous methanol solutions or neat water samples. Film growth was monitored by laser interferometry, which provides a direct measure of their thickness.[51] Sample compositions were targeted using Henry's law; however, vapor fractionation in the gas handling system increases the methanol concentration in the films somewhat compared to targeted values. Sample compositions in TEM experiments are thus only accurate to within a factor of 2. Transmission electron microscopy and diffraction measurements were performed on a fresh area of the sample in order to minimize the dose from the primary beam (60 keV, 5μA/cm^2).

III. Results and Discussion

A. Methanol Desorption Kinetics from H_2O−MeOH Binary Films. A quantitative understanding of the desorption kinetics from mixed molecular solids is required in order to infer concentration depth profiles from TDMS experiments.[52,53] Provided the sublimation of binary films proceeds layer-by-layer, desorption rates are determined by their surface composition and phase as well as their temperature. However, the surface layer concentration can be strongly coupled to the transport kinetics of the underlying layers in the bulk of the sample.[52] Therefore, to properly interpret TDMS data, the coupled diffusion−desorption kinetics that correlate the experimentally observed sublimation rates with the continuously evolving samples composition need to be quantitatively understood. To minimize the effects of interdiffusion on the desorption kinetics, binary films were synthesized by dosing simultaneously with the H_2O and MeOH molecular beams on the Pt(111) substrate at a temperature of 80 K. These growth conditions (surface temperature, angle of incidence, molecular beam flux)[51] are expected to yield dense films with vertical concentration profiles that are initially uniform throughout the samples thickness. The composition and thickness of the samples were easily controlled by independently adjusting the relative fluxes of the two molecular beams and the dose time. Samples grown under these conditions appeared initially amorphous based on their vibrational spectra (when grown by beam or background deposition on a Pt(111) substrate at $T = 80{-}120$ K, data not shown) and electron diffraction pattern (when grown by background deposition on an amorphous carbon or silica substrate at $T = 115$ K, data not shown).

To investigate how the methanol desorption rates from binary ice films depend on their composition, isothermal desorption rates for H_2O ($m/z = 18$ amu) and MeOH ($m/z = 31$ amu) were measured at a temperature of 160 K for a series of samples having different but initially homogeneous bulk concentrations. Representative spectra for a 880 ML thick film having an initial monolayer fraction of 0.055 ± 0.010 are reported in Figure 3. The H_2O desorption rate (squares, left ordinate) from the binary mixture is observed to follow near-zero-order kinetics, whereas the methanol desorption rate (circles, right ordinate) begins at a relatively high value but decays rapidly as sample desorption proceeds. While methanol diffusion in ice was qualified as being extremely slow,[10] the diffusion length in ice at 160 K is estimated to reach $L = (2Dt)^{1/2} \approx 220$ ML at $t = 800$ s using the kinetic parameters reported by Livingston et al.[21] For samples several hundred layers thick, a diffusion coefficient of this magnitude would cause significant continuous remixing of the methanol within the ice film during these TDMS experiments. Assuming rapid methanol bulk diffusion could maintain a relatively homogeneous instantaneous concentration throughout the film thickness, the rapid decrease in the methanol desorption rate during isothermal desorption experiments could therefore be interpreted in terms of the more volatile methanol fraction being preferentially depleted (i.e., fractionally distilled) from the sample. In this limit, the time-dependent methanol desorption rate should scale with the samples instantaneous bulk concentration for the whole duration of these isothermal desorption experiments. As the quantities of H_2O and MeOH

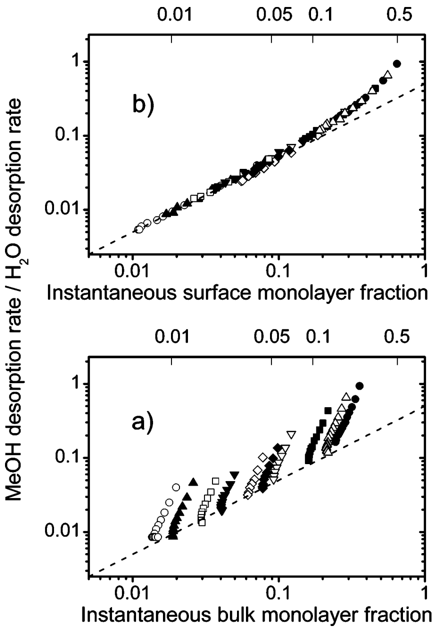

Figure 4. (a) Isothermal methanol desorption rates at 160 K (scaled by the instantaneous H_2O desorption rates to account for small differences in the isothermal desorption temperature) for 10 individual samples having different initially homogeneous bulk concentrations [initial MeOH monolayer fraction: (○) 0.022; (▲) 0.029; (□) 0.043; (▼) 0.057; (◇) 0.083; (◆) 0.107; (▽) 0.13; (■) 0.23; (△) 0.31; (●) 0.375] plotted as a function of their continuously evolving instantaneous bulk MeOH monolayer fractions. The top scale shows the corresponding approximate instantaneous bulk MeOH mole fractions (see text). (b) Same data as panel a but plotted as a function the samples continuously evolving instantaneous surface MeOH monolayer fraction. The top scale shows the corresponding approximate instantaneous surface MeOH mole fractions (see text). The dotted lines in panels a and b are a power law that shows the proportionality between the MeOH desorption rate and the samples instantaneous surface MeOH monolayer fraction for the smallest concentrations used in the present work.

that were initially deposited are known very accurately, the amounts of ice and methanol that remain on the substrate as a function of desorption time and the corresponding instantaneous bulk concentration can both be easily evaluated by integration of the experimentally determined desorption rates.

To quantitatively evaluate this interpretation, Figure 4a displays the instantaneous methanol desorption rates from binary H_2O−MeOH films having various initially homogeneous compositions (between 0.022 and 0.375 monolayer fractions) as a function of their continuously evolving instantaneous bulk MeOH monolayer fractions during isothermal desorption experiments similar to that shown in Figure 3. The methanol desorption rates have been normalized by the (relatively constant) water desorption rates to account for small differences (±50 mK) in the isothermal desorption temperature between individual experiments. The top axis shows the corresponding approximate instantaneous bulk MeOH mole fractions, x_{MeOH}. Instead of falling on the same line, the methanol desorption rates from individual samples are seen to decrease much more rapidly with their instantaneous bulk MeOH monolayer fractions than would be expected if diffusional remixing was able to maintain a homogeneous concentration distribution throughout the films thickness. This suggests that the methanol desorption rates from these mixed molecular solids are controlled by much slower bulk diffusion kinetics than those reported by Livingston et al.[21]

At the opposite limit, if MeOH translational diffusion was negligibly slow compared to the ice desorption rate, one would expect that the MeOH desorption rates should scale with the films continuously evolving instantaneous surface composition. As discussed previously, the amounts of ice and methanol that remain on the substrate as a function of desorption time are known very accurately, and the instantaneous surface concentration can therefore be easily evaluated from the experimentally determined desorption rates. In Figure 4b we recast the same MeOH desorption rates as in Figure 4a but here they are displayed as a function of the samples continuously evolving instantaneous surface MeOH monolayer fraction during the isothermal desorption experiments, thereby neglecting completely methanol translational diffusion. Again, the top axis shows the corresponding approximate instantaneous surface MeOH mole fraction. The MeOH desorption rates from films having various initially homogeneous concentrations map onto a single curve of MeOH desorption rate versus instantaneous surface MeOH monolayer fraction. The dotted line on the power plots (Figure 4a and 4b) shows how at small concentrations (i.e., monolayer fractions < 0.1) the MeOH desorption rate at 160 K from MeOH−H_2O binary films is proportional to (i.e., displays first-order kinetics with respect to) their instantaneous surface MeOH monolayer fractions. This observation that the instantaneous isothermal MeOH desorption rates from thin binary films are determined by the instantaneous composition of their surface layer requires that the MeOH diffusion rates are much smaller than those previously reported.[21] Furthermore, assuming layer-by-layer desorption of these mixed molecular solid films, these observations indicate that their isothermal methanol desorption rates can therefore be used to determine the samples continuously evolving instantaneous surface compositions (i.e., their MeOH monolayer fractions). Therefore, for volatile impurities that display very slow transport kinetics in ice such as methanol, this allows us to perform isothermal desorption depth profiling analyses to obtain their concentration depth profiles in thin ice films.

The slow transport kinetics for methanol in ice implied by these observations and the proportionality of its desorption rate to the sample's instantaneous surface MeOH monolayer fraction therefore enable us to interpret the isothermal desorption rates from initially homogeneous binary films (i.e., Figure 3) in terms of a much larger methanol concentration in the films superficial few tens of monolayers. The observation that, at the beginning of the TDMS experiment, the MeOH desorption rates (Figure 4a, symbols) are always much larger than expected from the films instantaneous bulk MeOH monolayer fraction (Figure 4a, dotted line) also supports this conclusion. This is in contrast with our assumption of an initially homogeneous concentration within the samples resulting from simultaneous dosing of H_2O and MeOH vapors on Pt(111) at 80 K with the two molecular beams. Qualitatively similar desorption profiles were also obtained from identically prepared specimens 200−2000 ML thick grown at temperatures in the 35−110 K range. However, FTIR analyses performed during sample growth and subsequent isothermal desorption experiments indicated that the initially amorphous mixed molecular solid films crystallized much faster upon heating to the isothermal desorption temperature of 160 K than neat amorphous H_2O films (data not shown). Large-scale (transient) molecular transport has previously been observed to occur concomitantly with similar phase transformations.[54] It was interpreted to proceed by percolation of impurity molecules through extended interconnected pathways (cracks) that transiently appear in the crystallizing film due to stress-induced fractures arising from the different densities of the mother and daughter solid phases.[54] Alternatively, extensive transient mobility may also have occurred in the (much more fluid) amorphous phase[55] prior to its crystallization to cubic ice I_c (section III.C). We therefore hypothesize that the larger methanol concentration in the near-surface region of the initially homogeneous binary films developed either prior to or during crystallization of the samples but that the methanol transport kinetics in the resulting crystallized film remained very slow thereafter, resulting in negligible further continuous intermixing during the isothermal desorption experiments at 160 K. The simple desorption kinetics displayed by dilute methanol-doped ice films and their slow transport kinetics therefore yield a straightforward interpretation of the isothermal desorption rates in terms of their one-dimensional concentration depth profiles. In the next section, this observation is used to quantify the molecular diffusion kinetics for methanol in polycrystalline ice.

B. Diffusion Kinetics for Methanol in Layered, Polycrystalline Binary Ice Films. To quantify the methanol transport kinetics in ice, laminated samples (i.e., H_2O/MeOH/H_2O layered films) were prepared on the Pt(111) substrate by sequential dosing of H_2O and MeOH vapors. First, several hundred layers of H_2O were deposited on the substrate, either with the H_2O beam doser (MB1) or by background deposition at pressures in the $10^{-7}-10^{-6}$ Torr range. For the adsorption fluxes used in the present work, crystalline ice samples formed on Pt(111) for temperatures above 145 K, while dense amorphous solid water (ASW) films were created by dosing H_2O at near normal incidence with a molecular beam for temperatures below 120 K.[23,24] Identical results were obtained by adsorbing H_2O vapor using background deposition at sample temperatures between 80 and 120 K, conditions that are also known to yield dense ASW films on Pt(111).[51] In a few selected experiments, polycrystalline underlayers were created by heating ASW films to temperatures greater than their glass-transition temperature, $T_g \approx 136$ K, thereby inducing crystallization by a nucleation and growth mechanism.[56] The sample phase was qualitatively evaluated (i.e., crystalline versus amorphous) using FTIR on Pt(111) and determined (i.e., cubic versus hexagonal polymorph) in separate experiments using electron diffraction on amorphous carbon or silica films (section III.C). ASW films grown on Pt(111) using similar procedures were shown to be dense and relatively smooth[57] and to kinetically wet the metal substrate for temperatures below 120 K.[58] However, it was recently reported that wetting may be compromised for thin ice films (i.e., tens of layers thick) grown on Pt(111) at temperatures above 125 K and during their isothermal desorption at 155 K.[58] Surprisingly, it was also observed that even after these films had crystallized, they continued to display apparent zero-order desorption kinetics despite the fact that they had dewetted the first H_2O bilayer on Pt(111).[58] However, as dewetting kinetics scale with the fifth power of the film thickness,[59] they are thus expected to slow dramatically for the much thicker samples used in this study (section III.C). Therefore, it can be argued that they probably did not interfere significantly with the desorption kinetics measurements reported here for relatively thick films on Pt(111).

A layer of methanol, whose thickness ranged from submonolayer to several ML, was then applied on top of this ice underlayer at temperatures between 35 and 120 K and at a 45° incidence angle using another molecular beam source (MB2). The upper temperature limit was determined by the condensation kinetics of methanol at the experimentally achievable fluxes. The sticking coefficient for methanol on ice below 120 K was observed to be unity within our detection limit. As the MeOH beam overfills the sample by less than 10%, only very small amounts of methanol adsorbed on other surfaces than the Pt(111) substrate.

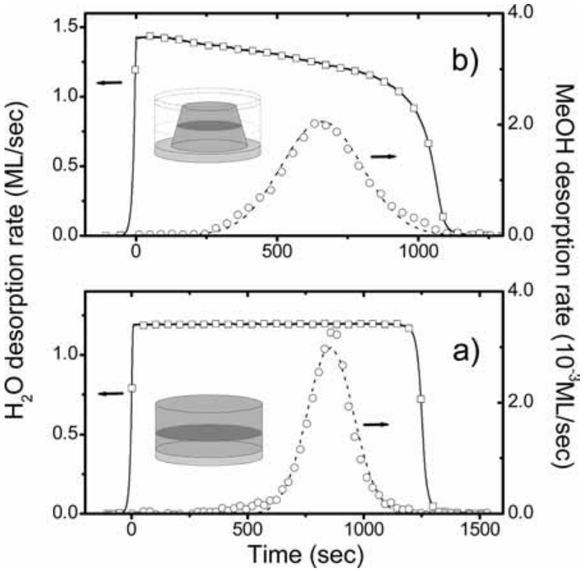

Figure 5. (a) Isothermal desorption rates for H_2O (□, left ordinate) and MeOH (○, right ordinate) at ca. 160 K for a 1500 ML thick binary film sample constructed by sequential dosing of 500 ML of H_2O, 0.75 ML of MeOH, and 1000 ML of H_2O using two molecular beams. (b) Isothermal desorption rates for H_2O (□, left ordinate) and MeOH (○, right ordinate) at ca. 160 K for a sample that was constructed identically to that described in panel a but was annealed at 170 K for 30 min in front of the glass slide prior to the TDMS experiment. Insets show schematics of the samples geometry.

The last step in the laminated film sample preparation procedure was to cap the methanol layer with several hundred additional layers of H_2O. It was observed that adsorption of H_2O on top of the methanol layer needed to be performed at substrate temperatures under 80 K in order to avoid intermixing of the methanol impurity layer with the H_2O overlayers.[60,61] At temperatures higher than 80 K, interdiffusion, competitive adsorption, and surface energy minimization effects cause methanol molecules to “float” (i.e., segregate) to the surface of the film during adsorption of the H_2O adlayers. Therefore, the capping H_2O layers were always deposited at normal incidence with the H_2O molecular beam doser at a substrate temperature between 35 and 80 K. Identical results were obtained by backfilling the chamber with $10^{-7}-10^{-6}$ Torr H_2O vapor at a substrate temperature of 80 K, both methods being known to yield dense ASW overlayers on ice and Pt(111) substrates for conditions used in the present work.[23,24,51]

Isothermal H_2O and MeOH desorption rates at a temperature of 160 K for a sample composed of a 500 ML thick ASW underlayer, a 0.75 ML thick MeOH middle layer, and a 1000 ML thick ASW overlayer, all grown at 80 K and yielding an overall bulk monolayer fraction of ca. 5×10^{-4}, are displayed in Figure 5a. The inset shows a schematic of the sample geometry. The H_2O desorption rate (squares, left ordinate) is observed to follow near-zero-order kinetics, while the MeOH desorption rate (circles, right ordinate) appears as a broad Gaussian-like feature that peaks approximately 800 s after the isothermal desorption temperature of 160 K was reached (i.e., onset of constant H_2O desorption rate). Assuming that sample sublimation proceeds layer-by-layer for these presumably wetting films and given the nearly zero-order desorption kinetics displayed by H_2O, desorption times can be approximately interpreted in terms of the relative depth within the sample. Furthermore, exploiting the proportionality between the metha-

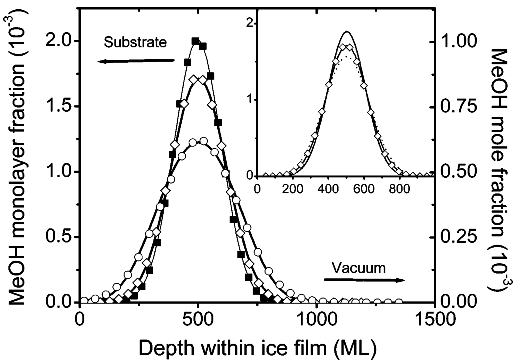

Figure 6. Methanol concentration depth profiles reconstructed from isothermal desorption experiments similar to those shown in Figure 5: (■) initial concentration profile, (◇) concentration profile after annealing for 30 min at 165 K, and (○) concentration profile after thermal annealing for 30 min at 170 K. Thick lines through open symbols represent simulation results of the diffusional spreading of the initial concentration profile (see text). (Inset) Comparison of the results of three numerical solutions of the one-dimensional diffusion equation using convolution integrals on the initial concentration profile (see text) for $D = 1 \times 10^{-15}$, 2.5×10^{-15}, and 5×10^{-15} cm^2 s^{-1} with the concentration profile obtained after thermal annealing for 30 min at 165 K (◇).

nol desorption rate and its instantaneous surface monolayer fraction at these small concentrations (section III.A) and neglecting the translational diffusion of methanol in ice at $T =$ 160 K,[62] the isothermal desorption rates displayed in Figure 5a can be interpreted in terms of a concentration depth profile. The resulting initial MeOH concentration depth profile was thus easily reconstructed from the experimentally determined desorption rates and is shown as the full line with black squares in Figure 6.

While the peak in the methanol concentration profile is estimated to be centered near where it was originally located during sample preparation (i.e., 500 ML from the film−substrate interface), the full width at half-maximum of the concentration depth profile is estimated to be close to 250 ML. This breadth is much larger than either the initial MeOH layer thickness (i.e., 0.75 ML) or the estimated film roughness (i.e., root-mean-squared roughness of at most a few tens of ML assuming stochastic growth at 80 K for ASW films from H_2O vapor).[57] Several factors could account for this large initial breadth such as thermal gradients, roughness of the interface, diffusional spreading, etc. To verify that these experimental artifacts did not distort the initial concentration profiles significantly, we performed isothermal desorption depth profiling experiments on four different laminated films of 1000 ML total thickness but where the 2 ML thick MeOH impurity layer was located 200, 400, 600, and 800 ML from the film−substrate interface. The reconstructed concentration depth profiles are reported in Figure 7a. The MeOH concentration profiles have very similar shapes and amplitudes but appear translated by the relative depth within the ice film that was selected during sample preparation. Their symmetrical shapes and relatively constant widths indicate that the unexpected large breadth of the initial concentration profiles does not arise from diffusional spreading that occurs during the isothermal desorption experiment.[62] To further establish this, we translated the experimental profiles by this known thickness, and Figure 7b shows that they overlap perfectly within experimental error. This demonstrates that while thermal gradients, interfacial roughness, and diffusional spreading are undoubtedly present in our experiments, they do not distort the experimental desorption traces significantly and thus do not contribute to the breadth of the initial concentration profile to an appreciable extent.

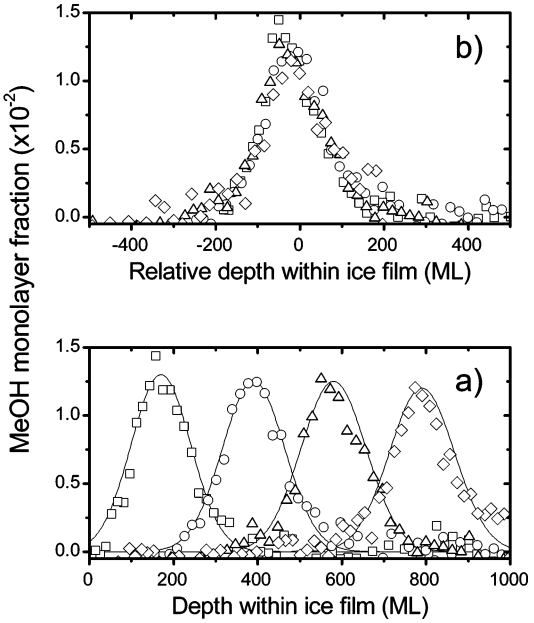

Figure 7. (a) Methanol concentration depth profiles for four different 1000 ML thick ice film samples where a 2 ML thick layer of MeOH was located 200 (□), 400 (○), 600 (△), and 800 ML (◇) from the film−substrate interface. (b) The same concentration profiles displayed in panel a were translated horizontally by their relative initial position within the ice film.

To understand the cause and nature of this unexpected large breadth of the initial concentration profile, experiments either where the ice underlayer was grown crystalline or where the ASW underlayer was crystallized prior to MeOH adsorption were performed (data not shown). The initial concentration profiles for these laminated samples were observed to be very asymmetric: they were much narrower on the crystalline ice bottom layer side (half-width at half-maximum ≈ 25 ML) than on the amorphous ice top layer side (half-width at half-maximum ≈ 150 ML). This suggests that the large breadth of the initial MeOH concentration profile is probably the result of a fast transient mobility that occurred upon heating of the sample to the isothermal desorption temperature of 160 K. This relatively rapid transient transport could have occurred either in the ASW phase prior to its crystallization[55] or through fissures during its transformation to polycrystalline ice (section III.C),[54] but the MeOH transport kinetics are observed to remain very slow in the crystallized sample during its isothermal desorption at 160 K (i.e., Figure 7).[62] Such a fast transient mobility was invoked in section III.A to explain the larger MeOH concentration observed in the first few tens of superfacial monolayers for films that were presumed to have initially homogeneous concentration profiles based on the sample growth conditions. This intriguing transient mobility and the resulting large breadth of the initial MeOH concentration profile are the main limiting factors that determines the smallest diffusion coefficient which could be investigated with our method.

In Figure 5b the isothermal H_2O (squares, left ordinate) and MeOH (circles, right ordinate) desorption rates from a laminated film that was prepared exactly as described before (i.e., for the sample shown in Figure 5a) are reported. However, this sample was annealed for 30 min at 170 K in front of the glass plate prior to the isothermal desorption depth profiling experiment. One notes that this sample would have completely desorbed in just over 2 min if thermal annealing had been carried out in the absence of the glass plate. The first observation is that the methanol desorption rate still follows a Gaussian-like shape but that it is much broader than that observed before thermal treatment (Figure 5a). The integral of the MeOH desorption rate indicates that only a small fraction (<10%) of the initial amount of methanol was lost during annealing. The second observation is that the water desorption rate does not follow the simple zero-order desorption kinetics displayed by a similarly prepared sample that did not undergo thermal annealing at high temperature (i.e., Figure 5a). Instead, the H_2O desorption rate decreases continuously during the isothermal desorption experiment. The tail region[26,63] toward the end of the isothermal desorption trace for H_2O also displays a more gradual decrease than that seen in Figure 5a.

Assuming that the desorption kinetics for H_2O and MeOH from binary films that were subjected to thermal annealing remain identical to those displayed by the sample in Figure 5a, various other physical factors need to be invoked to explain the apparent departures from simple zero-order H_2O desorption kinetics. For example, modifications in the sample geometrical integrity and shape during thermal annealing at 170 K in front of the glass plate could have occurred due to thermal gradients, nonhomogeneous desorption from the sample (mainly from its perimeter), surface roughening, dewetting, etc. These distortions in the sample morphology could cause apparent departures from zero-order H_2O desorption kinetics due to a continuous evolution in the sample geometry and consequently on its effective surface area, thereby affecting its macroscopic desorption rate during TDMS experiments. These geometrical artifacts must be accounted for in the reconstruction procedure in order to extract meaningful concentration depth profiles from samples that underwent thermal annealing at high temperature.

Using kinetic Monte Carlo simulations, we investigated the effects of the sample geometrical shape on the apparent desorption kinetics (data not shown). The most probable sample geometry that could account for experimental observations after thermal annealing is illustrated schematically in the inset of Figure 5b. It should be compared with the initial sample geometry before thermal annealing (dotted profile in inset to Figure 5b and inset to Figure 5a). This simple geometry accounts for the two most dramatic changes in the experimental desorption rates from the thermally annealed sample. First, the negative slope displayed by the H_2O isothermal desorption rate observed in Figure 5b could be explained in terms of a continuous modification in the aspect ratio of the sample as desorption proceeds resulting in a continuous decrease in its geometrical surface area. Second, the peak of the MeOH desorption trace (and thus of its concentration profile) appears relatively closer to the onset of the H_2O desorption trace (and thus the film−vacuum interface) than what is observed in Figure 5a. We therefore postulate that the sample sublimated partially, mainly at its periphery, during annealing at 170 K in front of the glass plate, yielding a slightly thinner film with a sample geometry that is significantly different than the initial cylindrical geometry. An increased roughness and/or a more rounded film topology could be responsible for the more progressive decrease in the H_2O desorption rate toward the end of the isothermal desorption experiment (i.e., tail region)[26,63] observed after annealing.

The MeOH concentration depth profiles obtained after thermal annealing were reconstructed using the procedure described above for the initial concentration depth profile by taking these trivial geometrical effects into consideration assuming the sample geometry illustrated in the inset. Representative results for two annealing temperatures are reported as open symbols in Figure 6 (open diamonds, 30 min annealing at 165 K, open circles, 30 min annealing at 170 K). One observes that the MeOH peak concentration decreases while the breadth of the distribution increases as diffusion spreads the initial concentration profile (full line with black squares). To extract heterodiffusion coefficients from these experimentally determined concentration depth profiles, they were least-squares fitted to simulations of the diffusionally broadened initial concentration profiles. These simulated concentration profiles were obtained by performing a convolution integral over the initial concentration depth profile providing a straightforward numerical solution to the one-dimensional diffusion equation. Representative results from this analysis are reported in the inset of Figure 6 for three different values of the diffusion coefficient [$D = 1 \times 10^{-15}$ cm^2/s (dotted line), $D = 2.5 \times 10^{-15}$ cm^2/s (full line), and $D = 5 \times 10^{-15}$ cm^2/s (dashed line)] and for a diffusion time of 30 min. Agreement between the simulated profile for $D = 2.5 \times 10^{-15}$ cm^2/s and the experimental data obtained after annealing the sample for 30 min at 165 K (open diamonds) is excellent. The best results from this analysis are displayed by thick continuous lines superimposed on the experimentally determined concentration profiles obtained after thermal annealing (open symbols) in Figure 6. This convolution integral procedure was performed to simulate the experimentally determined concentration profiles obtained from identically prepared films that were annealed for various times at several temperatures in the 145−195 K range yielding temperature-dependent heterodiffusion coefficients. For dilute solutions of MeOH in ice (mole fractions $< 10^{-3}$) and relatively short diffusion times, all experimentally determined concentration profiles agree very well with the simulated results that assume one-dimensional Fickian diffusion in an infinite homogeneous medium. These observations provide support to the interpretation of the diffusive nature for MeOH transport in ice and the concentration profiles reconstruction procedure, thereby providing reliable values for the MeOH heterodiffusion coefficients in thin ice films. Unfortunately, our knowledge of the sample microstructure and the quality of the data are insufficient to further interpret the apparent diffusion coefficients in terms of the classification introduced by Harrison[64] for diffusion in polycrystalline materials. Major sources of uncertainties are inaccuracies in the concentration depth profile reconstruction procedure (arising mainly from the uncertainties regarding distortions in sample geometry that occur during thermal annealing), the sample thickness, as well as inaccuracies in the convolution integral procedure. The absolute diffusion coefficients are thus estimated to be accurate to within ±100%. while the relative values have uncertainties smaller than ±25%.

Several control experiments were performed to further establish the diffusive nature of methanol transport in ice. Whereas in quantitative transport kinetics measurements thermal annealing was interrupted when the breadth of the concentration profile had only nearly doubled from its initial value (in order to avoid complications associated with the complex and unknown substrate−film and film−vacuum boundary conditions), a few series of experiments were carried out as a function of annealing time on a series of identically prepared samples. Unfortunately, the landmark square-root dependence of the diffusion length on the annealing time could not be observed unambiguously with the approach described here as it was masked by the large breadth of the initial concentration profile. Furthermore, strong departures of the experimentally determined concentration profiles from the simulated (i.e., Fickian) concentration profiles were observed for long diffusion times when

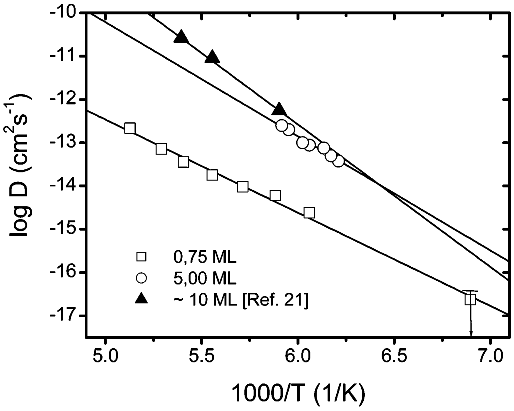

Figure 8. Arrhenius plot of the apparent diffusion coefficients for methanol in ice for three different methanol layer thicknesses in the laminate ice film samples: (□) 0.75, (○) 5.0, and (▲) ca. 10 ML.[21] Lines are least-squares regressions of the Arrhenius expression to the experimental data. Kinetic parameters are summarized in Table 1.

a significant amount of MeOH reached the interfaces as the simulations neglect the complex and unknown boundary conditions for diffusion in thin film samples. In these experiments methanol was observed to irreversibly adsorb on Pt(111) and segregate at the film−vacuum interface (section III.A). Transport kinetics measurements using a thicker methanol layer within the laminate film samples were also conducted revealing strong departures of the shape of the experimental concentration profiles from the simulated (i.e., Fickian) concentration profiles. This acute dependence of the transport kinetics on MeOH concentration is probably due to interferences by the phase separation and/or crystallization of other condensed phases[39] and their subsequent evolution within the polycrystalline ice film[21] and will be discussed further in section III.C.

The heterodiffusion coefficients obtained from analysis of experimental MeOH concentration depth profiles obtained from thermally annealed samples are displayed as a function of reciprocal annealing temperature in Figure 8. Data obtained for a MeOH layer thickness of 0.75 (open squares) and 5.0 ML (open circles) are compared with data from Livingston et al. (full triangles),[21] who reported an estimated methanol layer thickness of 10^8 molecules/μm^2 (i.e., approximately 10 ML).[44] Results for 0.50 and 0.75 ML MeOH layer thicknesses are identical within experimental error, suggesting that transport properties no longer depend on MeOH concentrations at the smallest thicknesses investigated in this study. From the summary of the experimental data displayed in Figure 8, it is concluded that the apparent heterodiffusion coefficient decreases dramatically (i.e., by more than a factor 10^3 at 185 K) with decreasing thickness of the methanol layer in the laminate film samples (i.e., from ∼10 ML to less than 1 ML thick). The temperature-dependent experimental data for each MeOH layer thickness were least-squares fitted to the Arrhenius relation in order to extract and compare kinetic parameters. The resulting diffusion preexponential factor, D_o, and activation energy, E_a, are reported for the various MeOH layer thicknesses in the laminate film structures in Table 1. It is observed that the apparent activation energy for diffusion decreases by more than 30% and that the apparent diffusion preexponential factor decreases by more than 9 orders of magnitude over the thickness range probed by the two investigations. This acute sensitivity of the transport kinetics on the concentration of methanol clearly highlights the strong coupling of the apparent transport kinetics with the complex phase behavior displayed by the more concentrated mixed molecular solids (section III.C).[39] This could very well explain some of the disagreements in the literature regarding transport properties of ice. In the next section, preliminary results on the morphology, phase, and microstructure of H_2O−MeOH binary films using TEM are presented.

TABLE 1. Summary of Arrhenius Kinetic Parameters for the Diffusion of Methanol in Ice Films

methanol layer thickness (ML)	temp. range (K)	D_o (cm^2 s^{-1})	E_a (kJ/mol)	ref
0.75	145−195	1.8×10^{-2}	41	this work
5.0	161−169	9.4×10^{2}	50.5	this work
10	169−185	2.4×10^{7}	63.6	21

It is instructive to compare our MeOH heterodiffusion coefficients with the recently reported H_2O self-diffusion coefficients in thin ice films in a similar temperature range.[65] These values for ultrathin films were reported to be a few orders of magnitude larger than low-temperature extrapolations of the self-diffusion coefficients for H_2O in macroscopic ice single-crystal samples (that proceed presumably by a self-interstitial diffusion mechanism) reported down to ∼220 K.[66,67] These apparently faster self-diffusion kinetics in thin ice films were hypothesized to arise from either a greater concentration of defects in thin ice films on Ru(001) compared to macroscopic single crystals or much faster transport kinetics in a liquidlike near-surface region of thin ice films.[65] The methanol heterodiffusion coefficients reported here are of comparable magnitude to the self-diffusion coefficients reported for thin ice films,[65] and thus, they are also a few orders of magnitude larger than the (extrapolated) self-diffusion coefficients of H_2O self-interstitials in pure ice single crystals.[66,67] However, due to uncertainties in the respective diffusion mechanisms and differences in sample microstructures, we believe further comment on the relative magnitude of the H_2O and MeOH diffusion coefficients in our thin polycrystalline ice films must await a more thorough understanding of these crucial parameters. However, impurity transport in polycrystalline ice has been observed to proceed faster through grain boundaries than (by a vacancy or an interstitial mechanism) through the crystalline lattice.[3,19] Therefore, experiments either where the ice underlayer was grown crystalline [i.e., grown at 145 K on Pt(111)] or where the ASW underlayers were crystallized (i.e., by annealing ASW at 160 K for a few seconds) prior to adsorption of the MeOH and ASW overlayers were also conducted. These preliminary investigations showed that the details of the ice preparation procedure (and thus the resulting sample morphology and microstructure) have a tremendous impact on the molecular transport properties of MeOH in ice. Detailed investigations of the dependence of the transport kinetics on the ice film microstructure are currently underway in our laboratory. However, these preliminary observations suggest that methanol heterodiffusion kinetics in single-crystalline ice may very well be even slower than the transport kinetics reported here for thin polycrystalline ice films.

C. Transmission Electron Microscopy and Diffraction of Methanol-Doped Ice Films. In separate experiments, the morphology, phase, and microstructure of pure and methanol-doped ice films were investigated using transmission electron microscopy. For conditions similar to those used for the growth of pure and binary samples on Pt(111) ($P = 10^{-6}$ Torr, $T =$ 115 K), relatively homogeneous thickness (i.e., flat and smooth) deposits were observed to grown on commercial amorphous carbon or silica films (SPI supplies Inc.). As expected, dewetting did not occur during prolonged annealing for neither pure nor methanol-doped homogeneous ASW films 300−1000 nm (1000−3000 ML) thick at temperatures in the 150−180 K range

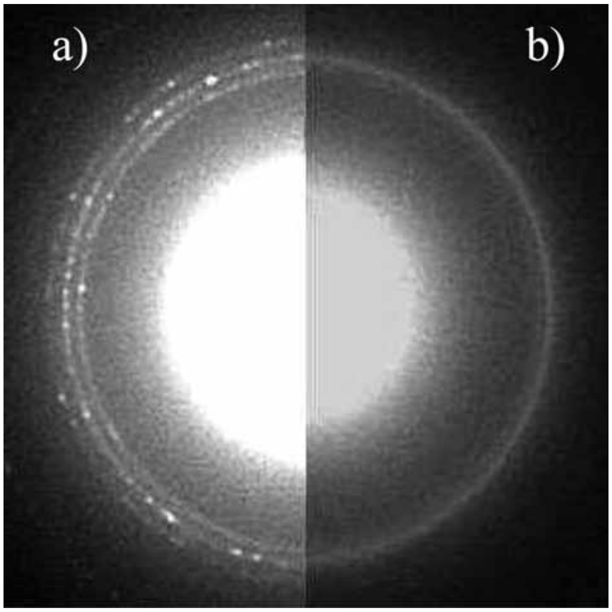

Figure 9. Electron diffraction patterns taken at 115 K for initially amorphous 600 nm (~2000 ML) thick binary $H_2O-MeOH$ films after thermal annealing at $T \approx 160$ K for 10 min for methanol mole fraction of (a) 5×10^{-2} and (b) 5×10^{-3}.

on either substrate. Dispersed individual ice crystallites are only observed during growth by background deposition at $T > 170$ K on these substrates. These observations suggest that the relatively thick film samples used in this study do not display a strong propensity toward dewetting or other morphological transformations for conditions used in the transport kinetics measurements. In agreement with previous studies,[68] annealing of pure ASW films above 160 K resulted in their crystallization to cubic ice I_c, whereas hexagonal ice I_h only appeared during annealing at $T > 180$ K or during growth by background deposition at higher H_2O partial pressures for $T > 180$ K. A detailed investigation of thin ice films physical properties as a function of growth conditions and thermal history will be reported in another publication.

In two separate experiments 600 nm (2000 ML) thick binary $H_2O-MeOH$ films having methanol concentrations of ca. 5×10^{-3} and 5×10^{-2} mole fractions were grown from the vapor pressure of binary aqueous solutions ($P = 10^{-6}$ Torr, $T = 115$ K, amorphous carbon film substrate). These samples were thus expected to have initially homogeneous MeOH concentrations, and electron diffraction indicated that they were initially amorphous. These two samples were then heated to $T \approx 160$ K for 10 min and cooled back down to 115 K, where their electron diffraction patterns, compared in Figure 9, were recorded on a fresh area of the sample with a CCD camera. The more dilute sample (Figure 9b) displays a diffraction pattern typical of polycrystalline (cubic) ice I_c.[68] Indistinguishable results were obtained for neat H_2O films prepared and annealed under identical conditions (data not shown). Interestingly, the electron diffraction pattern for the more concentrated sample (Figure 9a) is typical of polycrystalline (hexagonal) ice I_h.[68] No other phase[39] could be observed on amorphous carbon or silica substrates at the thicknesses, temperatures, and concentrations used in the transport kinetics experiments (section III.B). A detailed investigation of the phase behavior and associated kinetics for $H_2O-MeOH$ binary films is currently underway in our laboratory. However, it can be nonetheless concluded from these preliminary observations that the diffusion coefficients reported here describe methanol heterodiffusion in polycrystalline (cubic) ice I_c. Furthermore, it appears that methanol impurities, present above a certain threshold concentration, seem to promote crystallization of the hexagonal ice polymorph from ASW at much lower temperature than observed for neat ASW films. Ongoing investigations of the structural and morphological properties of pure and binary ice films are likely to reveal important aspects of their role in controlling the molecular transport properties of ice.

IV. Conclusions

We described how the simple desorption kinetics displayed by dilute methanol-doped polycrystalline (cubic) ice I_c can be interpreted in terms of a depth profiling analysis. Using a simple and original procedure to inhibit ice sublimation and this straightforward interpretation of the TDMS experiments in terms of concentration depth profiles we were able to probe the slow heterodiffusion kinetics for methanol in ice. We demonstrated the acute dependence of the apparent transport properties of thin ice films on the details of the sample preparation procedure and impurity concentration showing that great care must be exerted in quantifying these parameters and in interpretation of the complex coupled kinetics for desorption and transport. The apparent heterodiffusion kinetics for methanol, despite being much slower than previously reported, are still a few orders of magnitude faster than extrapolations of self-diffusion kinetics in macroscopic ice single crystals. However, preliminary work indicated that methanol diffusion through an initially crystalline underlayer appeared slower yet. Therefore, we believe the heterodiffusion kinetics reported here are probably affected by rapid transport through grain boundaries in the polycrystalline ice films. A more detailed understanding of the sample microstructure is required to further interpret the observed kinetics in terms of a diffusion mechanism, and work in this direction is underway in our laboratory.

Acknowledgment. We thank NSERC, FQRNT, CFI, and the Université de Sherbrooke for financial support as well as the Université de Sherbrooke machine shop for their assistance in building the instrument used for this work. We also thank Derek Hopkins of the Instrument Development Laboratory at PNNL for technical support and Dr. Bruce Kay and Dr. Zdenek Dohnalek for insightful discussions. Assistance from Pierre-Luc Dallaire-Demers in the kinetic Monte Carlo simulations of the coupled diffusion-desorption kinetics is acknowledged.

References and Notes

(1) Petrenko, V. F.; Withworth, R. W. *Physics of ice*; Oxford University Press: Oxford, 1999.

(2) Augustin, L.; Barbante, C.; Barnes, P. R. F.; Barnola, J. M.; Bigler, M.; Castellano, E.; Cattani, O.; Chappellaz, J.; DahlJensen, D.; Delmonte, B.; Dreyfus, G.; Durand, G.; Falourd, S.; Fischer, H.; Fluckiger, J.; Hansson, M. E.; Huybrechts, P.; Jugie, R.; Johnsen, S. J.; Jouzel, J.; Kaufmann, P.; Kipfstuhl, J.; Lambert, F.; Lipenkov, V. Y.; Littot, G. V. C.; Longinelli, A.; Lorrain, R.; Maggi, V.; Masson-Delmotte, V.; Miller, H.; Mulvaney, R.; Oerlemans, J.; Oerter, H.; Orombelli, G.; Parrenin, F.; Peel, D. A.; Petit, J. R.; Raynaud, D.; Ritz, C.; Ruth, U.; Schwander, J.; Siegenthaler, U.; Souchez, R.; Stauffer, B.; Steffensen, J. P.; Stenni, B.; Stocker, T. F.; Tabacco, I. E.; Udisti, R.; van de Wal, R. S. W.; van den Broeke, M.; Weiss, J.; Wilhelms, F.; Winther, J. G.; Wolff, E. W.; Zucchelli, M. *Nature* **2004**, *429*, 623−628.

(3) Rempel, A. W.; Waddington, E. D.; Wettlaufer, J. S.; Worster, M. G. *Nature* **2001**, *411*, 568−571.

(4) Ikeda-Fukazawa, T.; Fukumizu, K.; Kawamura, K.; Aoki, S.; Nakazawa, T.; Hondo, T. *Earth Planet. Sci. Lett.* **2005**, *229*, 183−192.

(5) Abbatt, J. P. D. *Chem. Rev.* **2003**, *103*, 4783.

(6) Huthwelker, T.; Malmstrom, M. E.; Helleis, F.; Moortgat, G. K.; Peter, T. *J. Phys. Chem. A* **2004**, *108*, 6302−6318.

(7) Udistt, R.; Benassai, S.; Castellano, E.; Fattori, I.; Innocente, M.; Migliori, A.; Traversi, R.; Becagli, S. *Anal. Glacio.* **2004**, *39*, 53−61.

(8) Dominé, F.; Shepson, P. B. *Science* **2002**, *297*, 1506−1510.

(9) Sumner, A. L.; Shepson, P. B. *Nature* **1999**, *398*, 230−233.

(10) Ohno, H.; Igarashi, M.; Hondo, T. *Earth Planet. Sci. Lett.* **2005**, *232*, 171−178.

(11) Mulvaney, R.; Wolff, E. W.; Oates, K. *Nature* **1988**, *331*, 247−249.

(12) Flükiger, B.; Chaix, L.; Rossi, M. J. *J. Phys. Chem. A* **2000**, *104*, 11739.

(13) Aguzzi, A.; Flückiger, B.; Rossi, M. J. *Phys. Chem. Chem. Phys.* **2003**, *5*, 4157−4169.

(14) Livingston, F. E.; Smith, J. A.; George, S. M. *Anal. Chem.* **2000**, *72*, 5590.

(15) Dominé, F.; Xueref, I. *Anal. Chem.* **2001**, *73*, 4348−4353.

(16) Xueref, I.; Dominé, F. *Atmos. Chem. Phys.* **2003**, *3*, 1779−1789.

(17) Uras, N.; Devlin, J. P. *J. Phys. Chem. A* **2000**, *104*, 5770−5777.

(18) Devlin, J. P.; Gulluru, D. B.; Buch, V. *J. Phys. Chem. B* **2005**, *109*, 3392−3401.

(19) Thibert, E.; Dominé, F. *J. Phys. Chem. B* **1998**, *102*, 4432−4439.

(20) Thibert, E.; Dominé, F. *J. Phys. Chem. B* **1997**, *101*.

(21) Livingston, F.; Smith, J.; George, S. *J. Phys. Chem. A* **2002**, *106*, 6309−6318.

(22) Mishima, O.; Calvert, L. D.; Whalley, E. *Nature* **1984**, *310*, 393.

(23) Haq, S.; Harnett, J.; Hodgson, A. *Surf. Sci.* **2002**, *505*, 171−182.

(24) Stevenson, K. P.; Kimmel, G. A.; Dohnalek, Z.; Smith, R. S.; Kay, B. D. *Science* **1999**, *283*, 1505−1507.

(25) Smith, R. S.; Huang, C.; Wong, E. K. L.; Kay, B. D. *Surf. Sci.* **1996**, *367*, L13.

(26) Lofgren, P.; Ahlstrom, P.; Chakarov, D. V.; Lausmaa, J.; Kasemo, B. *Surf. Sci.* **1996**, *367*, L19−L25.

(27) Sadtchenko, V.; Ewing, G. E.; Nutt, D. R.; Stone, A. J. *Langmuir* **2002**, *18*, 4632−4636.

(28) Dounce, S. M.; Jen, S. H.; Yang, M.; Dai, H. L. *J. Chem. Phys.* **2005**, *122*.

(29) Baker, I. *J. Phys. Chem. B* **1997**, *101*, 6158.

(30) Kopp, M.; Barnaal, D. E.; Lowe, I. J. *J. Chem. Phys.* **1965**, *43*, 2965−2971.

(31) Hori, A.; Hondoh, T. *Can. J. Phys.* **2003**, *81*, 251−259.

(32) Itoh, H.; Kawamura, K.; Hondoh, T.; Mae, S. *J. Chem. Phys.* **1996**, *105*, 2408−2413.

(33) Ikeda-Fukazawa, T.; Horikawa, S.; Hondo, T.; Kawamura, K. *J. Chem. Phys.* **2002**, *117*, 3886−3896.

(34) Huber, C.; Beyerle, U.; Leuenberger, M.; Schwander, J.; Kipfer, R.; Spahni, R.; Severinghaus, J. P.; Weiler, K. *Earth Planet. Sci. Lett.* **2006**, *243*, 61−73.

(35) McNeill, V. F.; Loerting, T.; Geiger, F. M.; Trout, B. L.; Molina, M. J. *Proc. Nat. Acad. Sci.* **2006**, *103*, 9422−9427.

(36) Materer, N.; Starke, U.; Barbieri, A.; VanHove, M. A.; Somorjai, G. A.; Kroes, G. J.; Minot, C. *Surf.* Sci. **1997**, *381*, 190−210.

(37) Glebov, A.; Graham, A. P.; Menzel, A.; Toennies, J. P.; Senet, P. *J. Chem. Phys.* **2000**, *112*, 11011−11022.

(38) Ruan, C. Y.; Lobastov, V. A.; Vigliotti, F.; Chen, S. Y.; Zewail, A. H. *Science* **2004**, *304*, 80−84.

(39) Murthy, S. S. N. *J. Phys. Chem. A* **1999**, *103*, 7927.

(40) Blake, D.; Allamandola, L.; Sandford, S.; Hudgins, D.; Freund, F. *Science* **1991**, *254*, 548−551.

(41) Williams, K. D.; Devlin, J. P. *J. Mol. Struct.* **1997**, *416*, 277−286.

(42) Schlichting, H.; Menzel, D. *Rev. Sci. Instrum.* **1993**, *64*, 2013−2022.

(43) Daschbach, J. L.; Peden, B. M.; Smith, R. S.; Kay, B. D. *J. Chem. Phys.* **2004**, *120*, 1516−1523.

(44) Akhter, S.; White, J. *Surf. Sci.* **1986**, *167*, 101.

(45) Ogasawara, H.; Yoshinobu, J.; Kawai, M. *J. Chem. Phys.* **1999**, *111*, 7003.

(46) King, D. A.; Wells, M. G. *Surf. Sci.* **1972**, *29*, 454−482.

(47) Ayotte, P.; Hebert, M.; Marchand, P. *J. Chem. Phys.* **2005**, *123*.

(48) Mitlin, S.; Leung, K. T. *J. Phys. Chem. B* **2002**, *106*, 6234−6247.

(49) George, S. M.; Livingston, F. E. *Surf. Rev. Lett.* **1997**, *4*, 771−780.

(50) Haynes, D. R.; Tro, N. J.; George, S. M. *J. Phys. Chem.* **1992**, *96*, 8502−8509.

(51) Dohnalek, Z.; Kimmel, G. A.; Ayotte, P.; Smith, R. S.; Kay, B. D. *J. Chem. Phys.* **2003**, *118*, 364−372.

(52) Ayotte, P.; Smith, R. S.; Teeter, G.; Dohnalek, Z.; Kimmel, G. A.; Kay, B. D. *Phys. Rev. Lett.* **2002**, *88*.

(53) Mapes, M. K.; Swallen, S. F.; Kearns, K. L.; Ediger, M. D. *J. Chem. Phys.* **2006**, *124*, 054710.

(54) Smith, R. S.; Huang, C.; Wong, E. K. L.; Kay, B. D. *Phys. Rev. Lett.* **1997**, *79*, 909−912.

(55) Smith, R. S.; Kay, B. D. *Nature* **1999**, *398*, 788−791.

(56) Smith, R. S.; Huang, C.; Wong, E. K. L.; Kay, B. D. *Surf. Sci.* **1996**, *367*, L13−L18.

(57) Smith, R. S.; Dohnalek, Z.; Kimmel, G. A.; Stevenson, K. P.; Kay, B. D. *Chem. Phys.* **2000**, *258*, 291−305.

(58) Kimmel, G. A.; Petrik, N. G.; Dohnalek, Z.; Kay, B. D. *Phys. Rev. Lett.* **2005**, *95*, 166102.

(59) Brochard Wyart, F.; Daillant, J. *Can. J. Phys.* **1990**, *68*, 1084−1088.

(60) Souda, R.; Kawanowa, H.; Kondo, M.; Gotoh, Y. *J. Chem. Phys.* **2003**, *119*, 6194−6200.

(61) Souda, R. *Phys. Rev. Lett.* **2004**, *93*.

(62) The negligible effects of translational diffusion at the isothermal desorption temperature are justified a posteriori by the diffusion coefficients obtained below: the estimated diffusion length is $L < 30$ ML for $t = 800$ s at $T = 160$ K.

(63) Livingston, F. E.; Smith, J. A.; George, S. M. *Surf. Sci.* **1999**, *423*, 145−159.

(64) Harrison, L. G. *Trans. Faraday Soc.* **1961**, *57*.

(65) Livingston, F. E.; Whipple, G. C.; George, S. M. *J. Chem. Phys.* **1998**, *108*, 2197−2207.

(66) Onsager, L.; Runnels, L. K. *J. Chem. Phys.* **1969**, *50*, 1089−1103.

(67) Goto, K.; Hondoh, T.; Higashi, A. *Jpn. J. Appl. Phys.* **1986**, *25*, 351−357.

(68) Blackman, M.; Lisgarten, N. D. *Proc. R. Soc. A* **1956**, *239*, 93−107.